

Performance Improvements of Interleaving VRMs with Coupling Inductors

Pit-Leong Wong, *Student Member, IEEE*, Peng Xu, *Student Member, IEEE*, Bo Yang, and Fred C. Lee, *Fellow, IEEE*

Abstract—The multichannel interleaving buck converter with small inductance has proved to be suitable for voltage regulator modules (VRMs) with low voltages, high currents, and fast transients. Integrated magnetic components are used to reduce the size of the converter and improve efficiency. However, the structure of the integrated magnetic requires precise adjustment and is not mechanical stable. This paper proposes integrated coupling inductors between the channels to solve these problems. With the proper design, coupling inductors can improve both the steady-state and dynamic performances of VRMs with easier manufacturing.

Index Terms—Coupling inductors, interleaving VRMs.

I. INTRODUCTION

PROCESSORS of future computers are expected to demand low voltages, at about 1 V, and higher current consumptions with higher clock rates. The increasing steady-state and dynamic requirements impose challenges to the design of the voltage regulator modules (VRMs) in future computer power systems [7], [8].

In order to improve the transient responses, small inductances need to be used, which increases the steady-state current ripples. The large current ripples impose stresses to the output capacitor and increase the steady-state voltage ripples as well. In order to solve this problem, multichannel interleaving is used to reduce the current ripple to the output capacitors [3]–[5]. Multichannel interleaving VRMs have been widely adopted as industry practice. For simplicity, only two-channel interleaving is shown in Fig. 1.

Compared to single buck converters, the multichannel interleaving structure has more components. The number of MOSFETs is determined by the power level, losses, cost, etc. It should be designed to be similar in these two cases for fair comparison. The multichannel interleaving structure has more inductors than the single buck converters, which increases the complexity of this converter. Integrated magnetic components can reduce the core number and the complexity of converters [6]. The two individual inductors of the two interleaving channels can be integrated on a single pair of E-E or E-I cores to reduce component counts [2]. The two inductors are in the

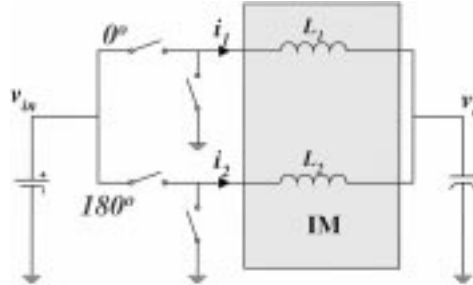


Fig. 1. Interleaving buck VRM.

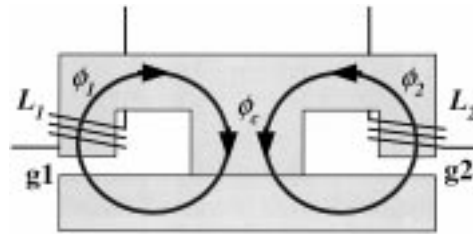


Fig. 2. Core structure of the integrated inductors.

shaded area in Fig. 1. The structure of the integrated inductor is shown in Fig. 2. The two inductors are built on the two outer legs of the core. Air gap is required on each outer leg to avoid saturation of the core. No air gap is used on the center leg, so that the two inductors can be decoupled. The fluxes generated by the two windings go through the center leg. Due to the phase shift in this interleaving structure, the ac magnetic flux ripple in the center leg can be reduced. Thus, the core loss of the center leg can be reduced, and the overall efficiency can be improved.

However, this kind of magnetic core is not a standard industry practice. The cores need to be precisely adjusted. The two pieces of the cores connect to each other only at the center leg. To ensure mechanical stability, gap filling must be used in the air gap of the two outer legs. Because no air gap is allowed in the center leg, the thicknesses of the gap fillings in the two outer legs must be precisely equal to the thicknesses of the air gaps. This makes mass production difficult and costly. Moreover, because the air gap cannot be adjusted to achieve different inductances, as it is in conventional inductor design, once the core is cut only one inductance value can be gotten. This also reduces the flexibility of the core.

Starting from the point of simplifying the core structure, this paper proposes coupling inductors between channels to improve both the steady-state and dynamic performances of the VRMs [1].

Manuscript received April 3, 2000; revised April 4, 2001. Recommended by Associate Editor C. K. Tse.

P.-L. Wong is with the Linear Technology Corporation, Milpitas, CA 95035 USA (e-mail: pitlwong@vpec.vt.edu).

P. Xu, B. Yang, and F. C. Lee are with the Virginia Polytechnic Institute and State University, Blacksburg, VA 24061 USA (e-mail: xupeng@vpec.vt.edu; boyang@vpec.vt.edu; fclee@vt.edu).

Publisher Item Identifier S 0885-8993(01)05960-9.

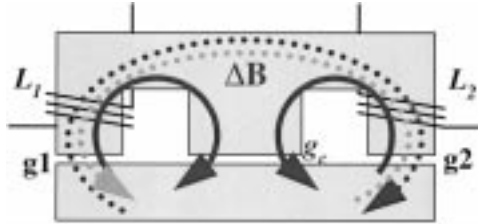


Fig. 3. Core structure of the proposed integrated inductors.

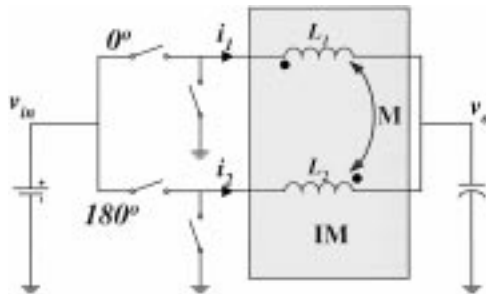


Fig. 4. Interleaving converter with coupling output inductors.

II. EFFECT OF COUPLING INDUCTORS ON CONVERTER PERFORMANCE

The core structure for the integrated inductors under analysis is shown in Fig. 3. The difference between this structure and the structure in Fig. 2 is the air gap in the center leg. With the air gap in the center leg, the thicknesses of the gap fillings of the two outer legs do not affect the mechanical stability of cores. They do not need to be very precise as they are in the decoupled core structure. Of course, they affect the inductances as they do in the conventional inductor structures. In this structure, the center leg is no longer a low magnetic reluctance path for the fluxes because of the air gap. The flux generated by the winding of L_1 can go through all three legs if the winding of L_2 is an open circuit. The flux generated by the winding of L_2 has a similar path. The flux interaction between the windings, the dotted line in Fig. 3, indicates the coupling effect between these two inductors. The following analyzes how the coupling effect affects the steady-state and dynamic performances of the converter.

Because of the coupling effect, the two inductors cannot be considered as two individual inductors, as in Fig. 1. A coupling inductance M between the two inductors can represent the coupling effect, as shown in Fig. 4.

The two inductors can be directly coupled or inversely coupled, due to the different direction selections between the two windings. There are two identical equivalent circuits for each coupling format, as shown in Fig. 5.

Both the two coupling formats can be described in (1). The difference is that the coupling inductance M is positive in direct coupling and negative in inverse coupling

$$\begin{cases} v_1 = L_1 \cdot \frac{di_1}{dt} + M \cdot \frac{di_2}{dt} \\ v_2 = M \cdot \frac{di_1}{dt} + L_2 \cdot \frac{di_2}{dt} \end{cases} \quad (1)$$

where v_1 and v_2 are the voltages applied on the two corresponding windings. There are two possible voltage values for

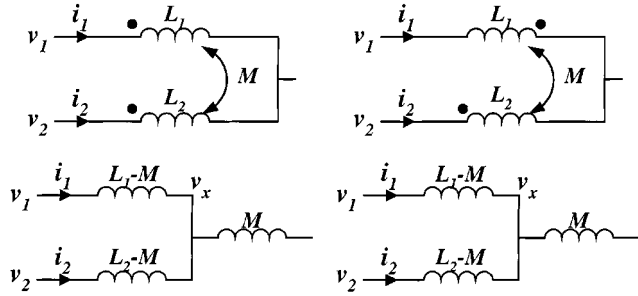


Fig. 5. Two different formats of the coupling inductors.

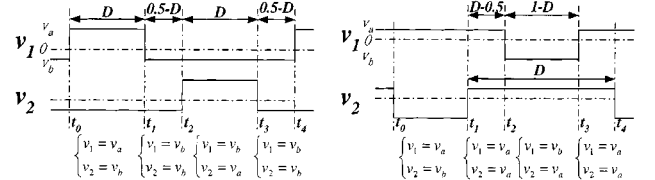


Fig. 6. Inductor voltage waveforms.

v_1 and v_2 : v_a , corresponding to the turn-on of the top switches; and v_b , corresponding to the turn-on of the bottom switches

$$\begin{cases} v_a = v_{in} - v_O > 0, \\ v_b = -v_O < 0. \end{cases} \quad (2)$$

The current i_2 in the first equation in (1) can be substituted by the second equation in (1). For the symmetric structure ($L_1 = L_2 = L$) and the definition $\alpha = M/L$, the first equation in (1) can be rewritten as (3)

$$(v_1 - \alpha \cdot v_2) = (1 - \alpha^2) \cdot L \cdot \frac{di_1}{dt}. \quad (3)$$

If the relationship between v_1 and v_2 can be found, (3) can be rewritten in the format of

$$v_1 = L_{eq} \cdot \frac{di_1}{dt}. \quad (4)$$

It is in the same format as the noncoupling inductors. The same format makes it easier to compare the performances of the two cases. The relationship between v_1 and v_2 changes at different time intervals during a switching cycle. Thus, during different time intervals, the equivalent inductance L_{eq} in (4) is different.

The waveforms of v_1 and v_2 for steady-state duty cycle ratio $D < 0.5$ and $D > 0.5$ are shown in Fig. 6(a) and (b), respectively. A switching cycle can be divided into four time periods. Because the voltage-second applied on the inductors balances for each cycle during the steady-state, there exists $D \cdot v_a = -D' \cdot v_b$ ($D' = 1 - D$). For both cases of steady-state duty cycle ratio $D < 0.5$ and $D > 0.5$, there are three different relationships between v_1 and v_2 in a switching cycle as shown in

$$\begin{cases} \begin{cases} v_1 = v_a \\ v_2 = v_b \end{cases} \Rightarrow v_2 = -\frac{D}{D'} v_1 \\ \begin{cases} v_1 = v_a \\ v_2 = v_a \end{cases} \text{ or } \begin{cases} v_1 = v_b \\ v_2 = v_b \end{cases} \Rightarrow v_2 = v_1 \\ \begin{cases} v_1 = v_b \\ v_2 = v_a \end{cases} \Rightarrow v_2 = -\frac{D'}{D} v_1. \end{cases} \quad (5)$$

For simplicity, same inductances are assumed in the two channels ($L_1 = L_2 = L$). Substituting the three relationships

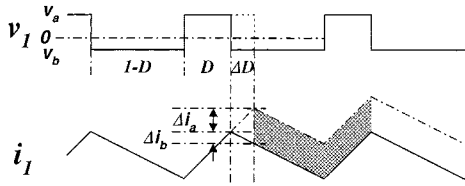


Fig. 7. Inductor voltage and current waveforms for the noncoupling case.

in (5) into (3), the corresponding equivalent inductances can be found, respectively, in (6), shown at the bottom of the page. There are totally three different equivalent inductances. L_{eq1} is defined for the time interval where $(v_1 > 0)$ and $(v_2 < 0)$, while L_{eq3} is for the time interval where $(v_1 < 0)$ and $(v_2 > 0)$. L_{eq1} is defined for the time interval where $(v_1 = v_2)$, no matter if they are positive or negative. Because both cases of steady-state duty cycle $D < 0.5$ and $D > 0.5$ have the same three relationships between v_1 and v_2 in a switching cycle, the equivalent inductances are the same for these two cases. For the low output voltage VRM applications, the steady-state duty cycle is less 0.5. The discussions in this paper are focused on the case of $D < 0.5$ to avoid lengthy repetition.

The interaction between channels due to the coupling effect can be represented by three different equivalent inductances in different time intervals. In the following part of this section, an analysis will show their contributions to the steady-state and dynamic performances of VRMs.

The voltage and current waveforms of noncoupling inductors are shown in Fig. 7. Because the channels work independently, only one channel is shown. The steady-state waveforms are the solid lines. From the waveform, the steady-state peak-to-peak current ripple can be described in (7). The dynamic response can be represented by an increase of the duty cycle of ΔD as the dotted line in Fig. 7. After one switching cycle, the inductor current increase due to the duty cycle increase is Δi_a and Δi_b , shown as the dot-dash line in Fig. 7. The relationship between the duty cycle increase and the current increase can be described in

$$I_{pp-nc} = \frac{V_a \cdot D}{L \cdot F_s}, \quad (7)$$

$$\left(\frac{\Delta i}{\Delta D} \right)_{nc} = \frac{\Delta i_a + \Delta i_b}{\Delta D} = \frac{V_{in}}{L \cdot F_s}. \quad (8)$$

For steady-state operation, a large inductance is preferred so that the current ripple can be reduced. Smaller current ripple gives smaller conduction losses in both the MOSFET and the filter capacitors. However, for the transient response, a small inductance is preferred so that a large current slew rate can be achieved. The steady-state and dynamic performances have contradictory requirements for the inductance. For noncoupling

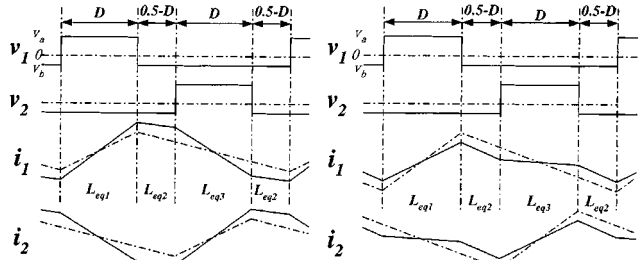


Fig. 8. Steady-state voltage and current waveforms for coupling inductors.

inductors, the steady-state performance has to be sacrificed to achieve a fast transient response.

For coupling inductors between interleaving channels, the inductor voltage and current waveforms for $M > 0$ or $M < 0$ and $D < 0.5$ or $D > 0.5$ are shown in Fig. 8, respectively. The coupling effects change the inductor current waveforms, as the solid line shown in Fig. 8. The current waveform for noncoupling inductors is also shown in Fig. 8 as the dot-dash line, for comparison. As shown in Fig. 6 and Formula (6), in the different time intervals of a switching cycle, the relationships between v_1 and v_2 are different, which results in different equivalent inductances in the different time intervals, as shown in Fig. 8. From the waveforms, for $D < 0.5$, the steady-state current ripple is determined by the equivalent inductance L_{eq1} . For the case of $D > 0.5$, the steady-state current ripple is determined by the equivalent inductance L_{eq3} . The equivalent inductance L_{eq1} or L_{eq3} is called “the steady-state equivalent inductance” for the case of $D < 0.5$ and $D > 0.5$, respectively. For $D < 0.5$. The relationship between the steady-state current ripple and the steady-state equivalent inductance is shown in

$$I_{pp-cp} = \frac{V_a \cdot D}{L_{eq1} \cdot F_s}. \quad (9)$$

From the equivalent inductances formulas in (6), it can be found that for $M > 0$, there always exists $L_{eq1} < L$, which results in a larger steady-state current ripple, as shown in Fig. 8(a) and

$$\begin{cases} v_2 = -\frac{D}{D'} v_1 \Rightarrow v_1 = \frac{1-\alpha^2}{1+\frac{D}{D'} \cdot \alpha} \cdot L \cdot \frac{di_1}{dt} \Rightarrow L_{eq1} = \frac{1-\alpha^2}{1+\frac{D}{D'} \cdot \alpha} \cdot L, \\ v_2 = v_1 \Rightarrow v_1 = (1+\alpha) \cdot L \cdot \frac{di_1}{dt} \Rightarrow L_{eq2} = (1+\alpha) \cdot L, \\ v_2 = -\frac{D'}{D} v_1 \Rightarrow v_1 = \frac{1-\alpha^2}{1+\frac{D'}{D} \cdot \alpha} \cdot L \cdot \frac{di_1}{dt} \Rightarrow L_{eq3} = \frac{1-\alpha^2}{1+\frac{D'}{D} \cdot \alpha} \cdot L. \end{cases} \quad (6)$$

(c). For $M < 0$, it is possible to have $L_{\text{eq}1} > L$. Let the expression of $L_{\text{eq}1}$ in (6) to be larger than L and solve the inequality. The condition to give $L_{\text{eq}1} > L$ can be found as shown in (10). In this case, the steady-state current ripple can be reduced, as compared to the noncoupling case. The steady-state current ripple reduction by inverse inductor coupling between interleaving channels is shown in Fig. 8(b)

$$-\alpha < \frac{D}{D'}. \quad (10)$$

Similarly, for $D > 0.5$, the condition to give $L_{\text{eq}3} > L$ is $-\alpha < D'/D$. In this case, the steady-state current ripple can be reduced as shown in Fig. 8(d).

The inductor voltage and current waveforms (both $M > 0$ and $M < 0$) for transient response analysis are shown in Fig. 9. Similar to the transient analysis of the noncoupling case, a duty cycle increase of ΔD is assumed during the transient response. After a switching cycle, the inductor current has an increase of Δi compared to the steady-state current. The transient response speed can be described by $\Delta i/\Delta D$. The difference between the coupling and noncoupling inductors is that the two channel need to be considered together in coupling inductors. Because the two interleaving channels use the same feedback control, it is reasonable to assume that the two channels have the same transient duty cycle increase of ΔD . The current increase is more complicated than that in the noncoupling inductors. The current increase Δi , which is the difference between the transient (the dashed lines) and steady-state (the solid lines) current waveforms, can be divided into different time intervals as shown in Fig. 9. Formula (11) is the summary of the current increase in different time intervals.

$$\left\{ \begin{array}{l} (t_0 - t_1) \mapsto \Delta i_1 = \left(\frac{v_a}{L_{\text{eq}1}} - \frac{v_b}{L_{\text{eq}2}} \right) \cdot \frac{\Delta D}{F_s}, \\ (t_1 - t_2) \mapsto \Delta i_2 = \left(\frac{v_b}{L_{\text{eq}2}} - \frac{v_b}{L_{\text{eq}2}} \right) \cdot \frac{(0.5-D-\Delta D)}{F_s} = 0, \\ (t_2 - t_3) \mapsto \Delta i_3 = \left(\frac{v_b}{L_{\text{eq}3}} - \frac{v_b}{L_{\text{eq}3}} \right) \cdot \frac{D}{F_s} = 0, \\ (t_3 - t_4) \mapsto \Delta i_4 = \left(\frac{v_b}{L_{\text{eq}3}} - \frac{v_b}{L_{\text{eq}2}} \right) \cdot \frac{\Delta D}{F_s}, \\ (t_4 - t_5) \mapsto \Delta i_5 = \left(\frac{v_b}{L_{\text{eq}2}} - \frac{v_b}{L_{\text{eq}2}} \right) \cdot \frac{(0.5-D-\Delta D)}{F_s} = 0. \end{array} \right. \quad (11)$$

The total current increase after one switching cycle is

$$\Delta i = \sum_{k=1}^5 \Delta i_k = \left(\frac{v_a}{L_{\text{eq}1}} - \frac{2 \cdot v_b}{L_{\text{eq}2}} + \frac{v_b}{L_{\text{eq}3}} \right) \cdot \frac{\Delta D}{F_s}. \quad (12)$$

During steady-state, The inductor currents are balanced in each switching cycle. From Fig. 8, it can be found that for both cases of steady-state duty cycle $D < 0.5$, there exists (13)

$$\frac{v_a}{L_{\text{eq}1}} \cdot D + \frac{v_b}{L_{\text{eq}2}} \cdot (1 - 2 \cdot D) + \frac{v_b}{L_{\text{eq}3}} \cdot D = 0. \quad (13)$$

Replacing $(v_b)/(L_{\text{eq}3})$ in (12) with (13), Formula (12) can be simplified as (14)

$$\Delta i = -\frac{1}{D} \cdot \frac{v_b \cdot \Delta D}{L_{\text{eq}2} \cdot F_s} = \frac{v_{\text{in}} \cdot \Delta D}{L_{\text{eq}2} \cdot F_s}. \quad (14)$$

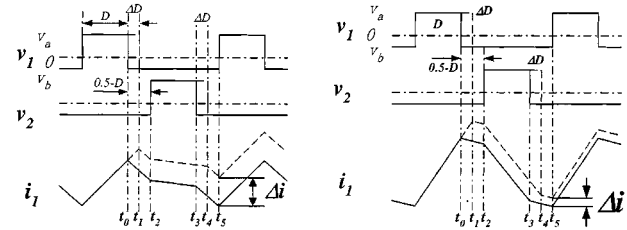


Fig. 9. Transient voltage and current waveforms for coupling inductors.

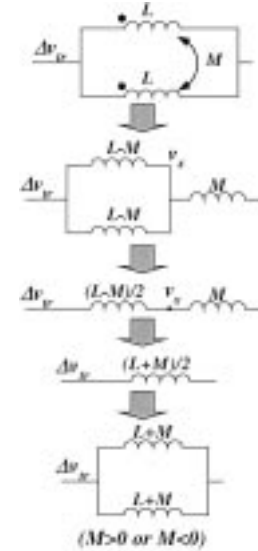


Fig. 10. Average small signal model of the coupled inductors.

Thus, the transient response speed can be described in (15)

$$\left(\frac{\Delta i}{\Delta D} \right)_{cp} = \frac{v_{\text{in}}}{L_{\text{eq}2} \cdot F_s}. \quad (15)$$

$L_{\text{eq}2}$ is the equivalent inductance during the time interval when $v_2 = v_1$. It is strange why the inductor current increases during transient response are only determined by it. This can be explained as follows. During the transients, the two channels have the same duty cycle changes. In average sense, this means the same amount of voltage changes at the two windings, which is $\Delta v_{\text{tr}} = v_{\text{in}} \cdot \Delta D$. When the same voltage applies to the two coupling inductors, the equivalent inductors are $L_{\text{eq}2}$. In average small-signal model, Δv_{tr} can be considered as a voltage perturbation. Because Δv_{tr} is the same for the two inductors, the two inductor can be connected together as shown in Fig. 10. This agrees with the definition of $L_{\text{eq}2}$. Thus, the inductor current increases of each inductor in one switching cycle due to the transient duty cycle changes follow (16), which is equivalent to (15)

$$\frac{\Delta i}{T_s} = \Delta i \cdot F_s = \frac{\Delta v_{\text{tr}}}{L_{\text{eq}2}} = \frac{v_{\text{in}} \cdot \Delta D}{L_{\text{eq}2}}. \quad (16)$$

The above average small-signal explanation of the inductor current increases is independent of the coupling inductance M , the steady-state duty cycle D , or the polarity of ΔD . Thus, (16) is valid for all the cases of $M > 0$ or $M < 0$ and $D > 0.5$ or $D < 0.5$. These can also be verified from the waveform analysis of the different cases, as shown in Fig. 9 and (11). Waveform

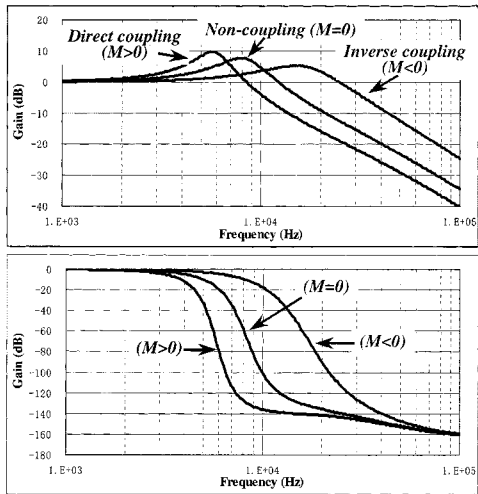


Fig. 11. Small signal model simulation of different coupling inductors.

analysis for other cases are not presented in this paper due to the consideration of paper length.

Because the dynamic performance of interleaving VRMs with coupling inductors is determined by L_{eq2} , the equivalent inductance L_{eq2} is called “the transient equivalent inductance.” To achieve a fast transient response, a smaller L_{eq2} is preferred. From Formula (6), there exists for $L_{eq2} < L$ for $M < 0$.

As discussed above, the transient equivalent inductance is the inductance that shows in the average small-signal model. The small-signal transfer functions can be another verification of the transient equivalent inductances. A two-channel interleaving VRM shown in Fig. 4 is simulated for small-signal transfer functions. The circuit simulation software used is SIMPLIS, which can give the small-signal bode plots directly from the switch circuit. Three cases with the same self-inductances but different mutual inductances are simulated. The control-to-output bode plots of the three cases ($M > 0$, $M = 0$, and $M < 0$) are compared in Fig. 11. It can be seen that the characteristic double poles of the Bode plots are determined by the transient equivalent inductance $L_{eq2} = (1 + \alpha) \cdot L$.

For coupling inductors between interleaving channels, the steady-state and dynamic performances of VRMs are determined by different equivalent inductances. Under certain conditions, both the steady-state and dynamic performances can be improved by adjusting corresponding equivalent inductances. However, for the noncoupling case, there is only one inductance ($L_{eq1} = L_{eq2} = L_{eq3} = L$), which makes it impossible to improve the steady-state and dynamic performances simultaneously. The possibility of improving both the steady-state and transient performances is the main benefit of applying coupling inductors in interleaving VRMs. The previous analysis shows that the inverse coupling inductors ($M < 0$) can improve both the steady-state and dynamic performances.

III. MAGNETIC DESIGN AND SIMULATION RESULTS

In this section, some simulation results and magnetic design are presented. The transient responses are determined by the

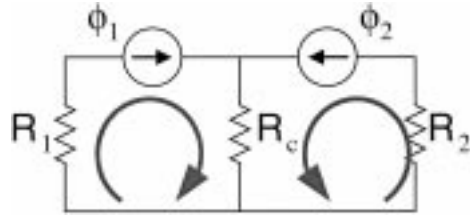


Fig. 12. Magnetic circuit for ac flux analysis.

transient equivalent inductance and the controller. To make fair comparison, the same controller should be used and the transient equivalent inductance should be designed to be the same for the noncoupling and coupling inductors. That is

$$L_{nc} = L_{eq2} = (1 + \alpha) \cdot L_{cp} \quad (17)$$

where L_{nc} is the inductance of the noncoupling case, while L_{cp} is the self-inductance of the coupling case. The following magnetic design comparison is based on this assumption.

Fig. 12 shows the magnetic analog circuit for the ac flux analysis of the core structure shown in Fig. 3. The magnetic reluctance of the three legs, R_1 , R_2 , and R_c can be determined by the following formula:

$$R_i = \sum_k \frac{l_k}{\mu_k \cdot A_k} \quad (i = 1, 2, c) \quad (18)$$

where

l_k length of the magnetic flux path;

μ_k corresponding permeability of materials in the flux path;

A_k corresponding cross-section area of the flux path.

The ac fluxes, ϕ_1 and ϕ_2 , are only determined by the voltage-second of the corresponding winding, as shown in Formula (19). Because the winding voltage-second is fixed, the ac flux is fixed. That is the reason the ac fluxes in the magnetic analog circuit can be represented by a current sources. No matter how the magnetic reluctance changes in the three legs, the ac fluxes in the three legs are the same as long as the voltage-second and the windings are the same. The simulation results of the inductor current and ac fluxes in the three legs for the inverse coupling case are shown in Figs. 13 and 14, respectively. Although the coupling effect changes the current waveforms in the inductors, it does not change the ac flux in the legs of the core

$$\begin{cases} \phi_1 = \int \frac{v_1}{N_1} dt, \\ \phi_2 = \int \frac{v_2}{N_2} dt. \end{cases} \quad (19)$$

The flux in the center leg, which is the sum of the fluxes in the outer legs, has a much smaller ripple. Thus, the core loss in the center leg can be reduced. The flux ripple cancellation effect is the same as that in the noncoupling cores. The previous analysis is based on the average flux viewpoint. The result can be different in finite element analysis. Fig. 15 shows the finite element analysis results of the ac magnetic flux distribution in the cores for different integrated inductor structures. The excitations of the windings are sinusoidal waves at the switching frequency. The magnitude of the sinusoidal waveform is the peak-to-peak

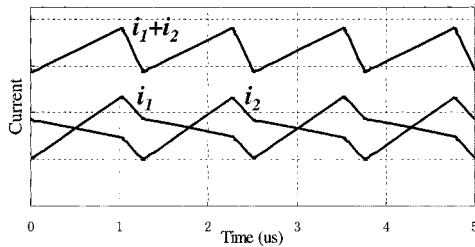


Fig. 13. Simulation current waveforms of inverse coupling inductors.

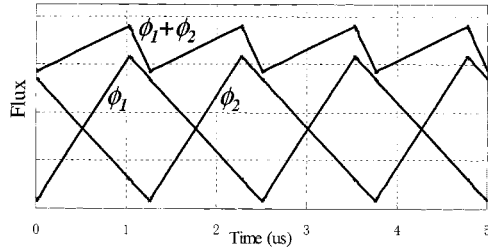


Fig. 14. Simulation flux waveforms of the core for inverse coupling inductors.

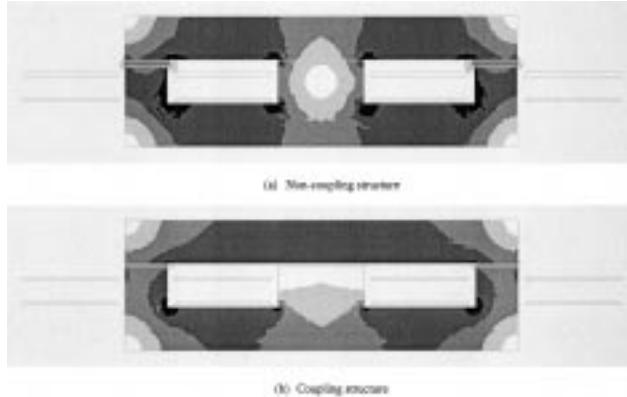


Fig. 15. Finite element analysis (FEA) flux distributions in the core.

value of the inductor current. The lighter color in Fig. 15 represents the lower ac flux density while the darker represents higher ac flux density.

In the noncoupling structure, although the average ac flux is zero in the center leg, there are still flux crowded areas. The low magnetic impedance in the center leg causes this uneven flux distribution. The areas crowded with ac flux generate large core losses, which are the hot spots in the core. In the inverse coupling structure, the air gap in the center leg increases the magnetic impedance, which makes the flux more evenly distributed in the center leg, as can be easily seen from Fig. 15. The inverse coupling structure is expected to have smaller magnetic core losses in the center leg than the noncoupling structure because of this even flux distribution.

For direct coupling, the flux in the center leg is the difference between ϕ_1 and ϕ_2 , $\phi_C = \phi_1 - \phi_2$. Because of the phase difference in interleaving channels, the ac flux magnitude is the sum of ϕ_1 and ϕ_2 . The magnetic core loss in the center leg is similar to that in the two outer legs. From the viewpoint of the core loss, there is no benefit for this inductor integration structure.

For the dc flux distribution analysis, the magnetic analog circuit is shown in Fig. 16.

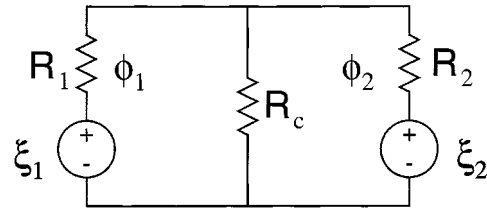


Fig. 16. Magnetic circuit for dc flux analysis.

Based on Ampere's law and the continuity of flux, for each loop in Fig. 16 there exists

$$\begin{cases} R_1 \cdot \phi_1 + R_c \cdot (\phi_1 + \phi_2) = N_1 \cdot i_1, \\ R_2 \cdot \phi_2 + R_c \cdot (\phi_1 + \phi_2) = N_2 \cdot i_2. \end{cases} \quad (20)$$

The flux of each outer leg can then be found

$$\begin{cases} \phi_1 = \frac{N_1 \cdot (R_2 + R_c)}{\Delta} \cdot i_1 - \frac{N_2 \cdot R_c}{\Delta} \cdot i_2, \\ \phi_2 = -\frac{N_1 \cdot R_c}{\Delta} \cdot i_1 + \frac{N_2 \cdot (R_1 + R_c)}{\Delta} \cdot i_2. \end{cases} \quad (21)$$

where

$$\Delta = R_1 \cdot R_2 + R_1 \cdot R_c + R_2 \cdot R_c. \quad (22)$$

The differential of (21) is

$$\begin{cases} v_1 = N_1 \cdot \frac{d\phi_1}{dt} = \frac{N_1^2 \cdot (R_2 + R_c)}{\Delta} \cdot \frac{di_1}{dt} - \frac{N_1 \cdot N_2 \cdot R_c}{\Delta} \cdot \frac{di_2}{dt}, \\ v_2 = N_2 \cdot \frac{d\phi_2}{dt} = -\frac{N_1 \cdot N_2 \cdot R_c}{\Delta} \cdot \frac{di_1}{dt} + \frac{N_2^2 \cdot (R_1 + R_c)}{\Delta} \cdot \frac{di_2}{dt}. \end{cases} \quad (23)$$

The inductance and the coupling effect between the two windings can be found by comparing (23) with (1). The relationship between the inductance and the magnetic reluctance is shown in

$$\begin{cases} L_1 = \frac{N_1^2 \cdot (R_2 + R_c)}{\Delta}, \\ L_2 = \frac{N_2^2 \cdot (R_1 + R_c)}{\Delta}, \\ M = \frac{N_1 \cdot N_2 \cdot R_c}{\Delta}. \end{cases} \quad (24)$$

For simplification, only symmetrical structure is further discussed. That is

$$\begin{cases} N_1 = N_2 = N, \\ R_1 = R_2 = R, \\ L_1 = L_2 = L. \end{cases} \quad (25)$$

Formula (24) can be simplified as (26)

$$\begin{cases} L = \frac{N^2 \cdot (R + R_c)}{R \cdot (R + 2 \cdot R_c)}, \\ M = -\frac{N^2 \cdot R_c}{R \cdot (R + 2 \cdot R_c)}, \\ \alpha = \frac{M}{L} = -\frac{R_c}{R + R_c}. \end{cases} \quad (26)$$

Formula (26) can be rewritten as (27), which are the magnetic design equations. For given self-inductance L and the coupling effect α , the magnetic reluctances of the outer and center legs are given in (27). For ferrite cores, the major reluctances are in the air gaps. Thus, the thickness of the air gaps can be derived from

$$\begin{cases} R = \frac{1}{1-\alpha} \cdot \frac{N^2}{L}, \\ R_c = \frac{-\alpha}{1-\alpha^2} \cdot \frac{N^2}{L}. \end{cases} \quad (27)$$

For inductor design, the dc flux bias is an important parameter. The following gives the dc fluxes in the three legs. Re-

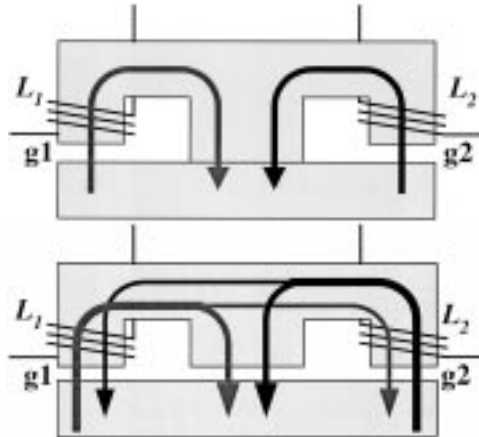


Fig. 17. DC flux distribution in the core.

placing the variables in (21) by their dc average counterparts, the dc flux bias in the outer legs for symmetric structure can be found as shown in (28) (assuming the dc current of the two windings are the same, $I_1 = I_2 = I$)

$$\Phi_1 = \Phi_2 = \frac{N}{R + 2 \cdot R_c} \cdot I. \quad (28)$$

Replacing R, R_c in (28) by the equations in (27), (28) can be rewritten in

$$\Phi_1 = \Phi_2 = \frac{(1 + \alpha) \cdot L \cdot I}{N} = \frac{L_{eq2} \cdot I}{N}. \quad (29)$$

The dc flux bias in the center leg is the sum of the dc fluxes in the two outer legs, $\Phi_c = \Phi_1 + \Phi_2$. A very important message in (29) is that the dc bias fluxes are determined by the transient equivalent inductance. For the noncoupling or coupling structures, as long as the transient equivalent inductances are designed to be the same, the dc fluxes bias in the core are the same for the same dc currents.

For the same core areas and winding turns, larger inductance usually results in larger dc flux bias. The inverse coupling structure ($-1 < \alpha < 0$) has larger self-inductance if it is designed to have the same transient equivalent inductance. However, due to the air gap in the center leg, the dc flux in the outer legs generated by the corresponding winding is partially cancelled by the dc flux generated by the other winding. The overall dc fluxes in the coupling core structure are the same as those in the noncoupling core structure if the transient equivalent inductances are designed to be the same for the two cases. The dc flux cancellation effect in coupling core structure is also explained in Fig. 17.

The purpose of the coupling core structure is to reduce steady-state current ripples while maintaining the transient responses. As shown in (7) and (9), the current ripples are determined by the steady-state equivalent inductance. If the noncoupling and coupling cases are designed to have the same transient equivalent inductances, the ratio of the peak-to-peak current in the inverse coupling inductors to that in the noncoupling inductors can be derived from (7), (9) and (17) as follows:

$$\frac{I_{pp-cp}(D<0.5)}{I_{pp-nc}} = \frac{L_{nc}}{L_{eq1}} = \frac{1 + \frac{D}{D'} \cdot \alpha}{1 - \alpha}. \quad (30)$$

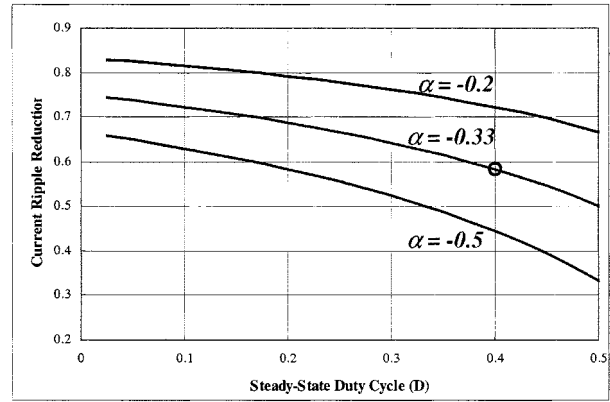


Fig. 18. Steady-state current ripple reduction effect for inverse coupling inductors.

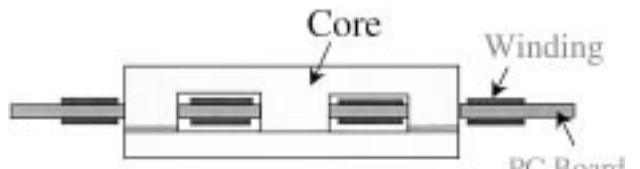


Fig. 19. PCB winding structure.

The steady-state current ripple reduction is a function of steady-state duty cycle and coupling effect. The relationship is shown in Fig. 18.

This section discusses the magnetic design of the inductors. The ac flux is cancelled in the center leg of the inverse coupling core structure. The dc fluxes in the inverse coupling core structure are partially cancelled. It is predicted that the core losses in the inverse coupling core structure can be reduced. The next section presents the experimental results to show the efficiency improvements of the coupling inductors.

IV. HARDWARE SETUP AND EXPERIMENTAL RESULTS

In order to make fair comparisons, the hardware of the noncoupling and inverse coupling inductors is kept as similar as possible. As discussed previously, the designs of same transient equivalent inductance give the most similar circuits for the two cases. With this design, the small-signal model for the noncoupling and coupling inductors are the same so that the same compensator can be used. Actually, the whole circuits including the windings are the same. The only difference is the air gap in the center leg.

The hardware is a four-channel interleaving synchronous buck VRM. Totally, two pairs of E-I cores are used in a circuit. The two channels with phase shift of 0° and 180° share a pair of cores, while the two channels with phase shift of 90° and 270° share another pair of cores. The E and I cores used are E18/4/10 and PLT 18/10/2 cores from Philips, respectively. The materials for all the cores are 3F3. Each inductor has two turns of winding. The windings are built on the two sides of the PCB. Each side has one turn. The cross section of the cores and the PCB windings are shown in Fig. 19. The circuit operation condition of the hardware is $F_s = 300$ kHz, $V_{in} = 5$ V,

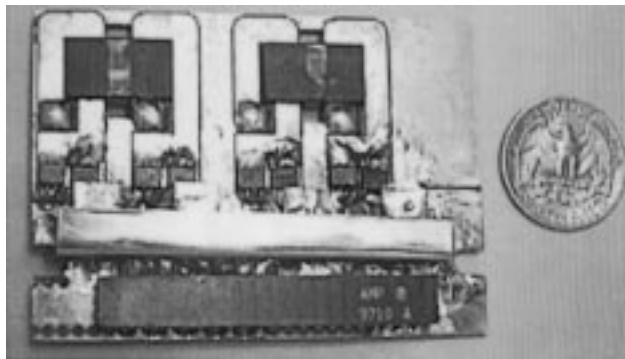


Fig. 20. Hardware under experimental comparison.

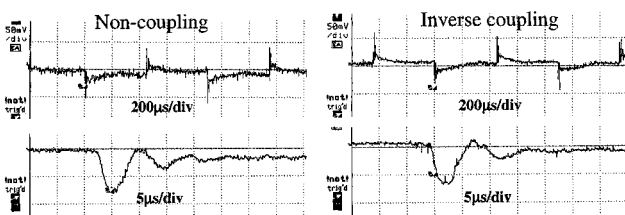


Fig. 21. Transient response comparison.

$V_o = 2$ V, and $I_o = 30$ A. The switches used in the circuit are Si4410 MOSFETs from Siliconix Inc. Each top and bottom switch in one channel uses one MOSFET, respectively. Totally, there are eight MOSFETs in the four-channel interleaving VRM. The output capacitors consist of two 470 μ F Tantalum capacitors and twenty-six 10 μ F ceramic capacitors.

For the noncoupling case, the inductance in each channel is 320 nH. The two outer legs of the E core need to be milled to generate the air gaps in the outer legs as shown in Fig. 2. For the inverse coupling case, the air gaps in the three legs are the same. The reason is that this is the simplest structure. The cores do not need to be milled. The cross section area of the center leg is twice of those of the outer legs, which gives $R = 2 \cdot R_c$. From (26), there exists $\alpha = -1/3$. The transient equivalent inductance of the inverse coupling cases is also 320 nH. Thus, the self-inductance is 480 nH. The operation point is marked in Fig. 18. The peak-to-peak current ripple can be reduced to below 60% compared to the noncoupling case.

The picture of the hardware is shown in Fig. 20. In fact, there are only one PCB layout and one controller. For the experiments of the noncoupling or coupling inductors, the cores on the PCB are changed.

The transient responses of the noncoupling and inverse coupling inductors shown in Fig. 21 have the same transient responses as expected. The efficiency comparison of the two cases is shown in Fig. 22. With inverse coupling inductors, efficiency can be improved by 2% at full loads and by 10% at light loads. The winding and core temperature comparisons are shown in Fig. 23. Coupling inductors reduce the core and winding temperatures about 5 °C. All the experimental data are obtained at room temperature without fan cooling.

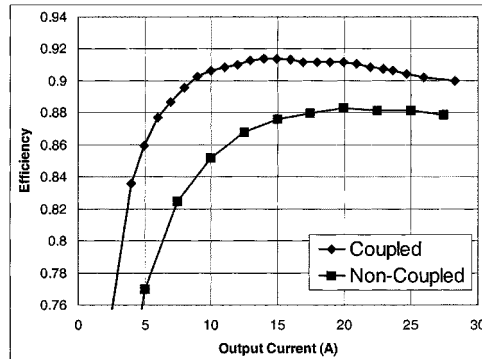


Fig. 22. Efficiency comparison.

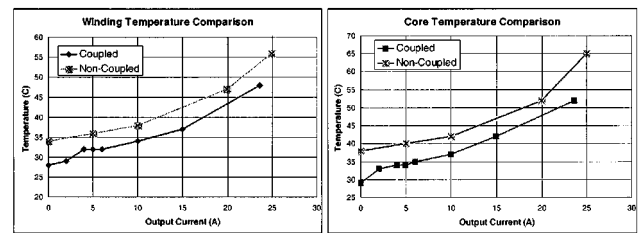


Fig. 23. Winding and core temperature comparison.

V. CONCLUSION

This paper proposes integrated coupling inductors in multi-channel interleaving VRMs. Coupling inductors have different equivalent inductances for steady-state and transient responses. With proper design, the inverse coupling inductors reduce the steady-state current ripple while maintaining the same transient response. The conduction losses in the MOSFETs can thus be reduced. The air gap in the center leg more evenly distributes the flux, which can reduce the core loss in the center leg. Experimental results show that the efficiency improvement due to inverse coupling inductors can be 2% at full loads and by 10% at light loads. Moreover, the coupling inductor core structures make the manufacture of the cores easier and improve the mechanical stability of the cores.

REFERENCES

- [1] P. Wong, Q. Wu, P. Xu, B. Yang, and F. C. Lee, "Investigating coupling inductors in the interleaving QSW VRM," in *Proc. APEC'00*, 2000, pp. 973–978.
- [2] W. Chen, F. C. Lee, X. Zhou, and P. Xu, "Integrated planar inductor scheme for multimodule interleaved quasi-square-wave (QSW) dc/dc converter," in *Proc. PESC'99*, 1999, pp. 759–762.
- [3] X. Zhou, P. Xu, and F. C. Lee, "A high power density, high efficiency and fast transient voltage regulator module with a novel current sensing and current sharing technique," in *Proc. APEC'99*, 1999, pp. 289–294.
- [4] P. Wong, F. C. Lee, X. Zhou, and J. Chen, "Voltage regulator module (VRM) transient modeling and analysis," in *Proc. IAS'99*, 1999, pp. 1699–1706.
- [5] X. Zhou, X. Zhang, J. Liu, P. Wong, J. Chen, H. Wu, L. Amoroso, F. C. Lee, and D. Y. Chen, "Investigation of candidate VRM topology for future microprocessors," in *Proc. APEC'98*, 1998, pp. 145–150.
- [6] W. Chen, G. Hua, D. Sable, and F. C. Lee, "Design of high efficiency, low profile low voltage converter with integrated magnetics," in *Proc. Virginia Power Electron. Center (VPEC) Sem.*, 1997, pp. 15–21.

- [7] S. Goodfellow and D. Weiss, "Design power systems around processor specifications," *Electron. Design*, pp. 53–57, Jan. 1997.
- [8] M. Zhang, M. Jovanovic, and F. C. Lee, "Design considerations for low-voltage on-board dc/dc modules for next generations of data processing circuits," *IEEE Trans. Power Electron.*, vol. 11, pp. 328–337, Mar. 1996.



Pit-Leong Wong (S'99) received the B.E. degree in control and B.S. degree in physics, and the M.S. degree in systems engineering from Tsinghua University, Beijing, China, in 1994 and 1996, respectively, and the Ph.D. degree from the Virginia Polytechnic Institute and State University, Blacksburg, in 2001.

He is with Linear Technology Corporation, Milpitas, CA. His research interests include design of low-voltage dc/dc converters, power factor correction techniques, distributed power system, magnetics, and modeling and control of converters.

Mr. Wong is a member of Phi Kappa Phi.

Fred C. Lee (S'72–M'74–SM'87–F'90) received the B.S. degree in electrical engineering from the National Cheng Kung University, Taiwan, R.O.C., in 1968 and the M.S. and Ph.D. degrees in electrical engineering from Duke University, Durham, NC, in 1971 and 1974, respectively.

He is a University Distinguished Professor with Virginia Polytechnic Institute and State University (Virginia Tech), Blacksburg, and previously was the Lewis A. Hester Chair of Engineering at Virginia Tech. He directs the Center for Power Electronics

Systems (CPES), a National Science Foundation engineering research center whose participants include five universities and over 100 corporations. In addition to Virginia Tech, participating CPES universities are the University of Wisconsin-Madison, Rensselaer Polytechnic Institute, North Carolina A&T State University, and the University of Puerto Rico-Mayaguez. He is also the Founder and Director of the Virginia Power Electronics Center (VPEC), one of the largest university-based power electronics research centers in the country. VPEC's Industry-University Partnership Program provides an effective mechanism for technology transfer, and an opportunity for industries to profit from VPEC's research results. VPEC's programs have been able to attract world-renowned faculty and visiting professors to Virginia Tech who, in turn, attract an excellent cadre of undergraduate and graduate students. Total sponsored research funding secured by him over the last 20 years exceeds \$35 million. His research interests include high-frequency power conversion, distributed power systems, space power systems, power factor correction techniques, electronics packaging, high-frequency magnetics, device characterization, and modeling and control of converters. He holds 19 U.S. patents, and has published over 120 journal articles in refereed journals and more than 300 technical papers in conference proceedings.

Dr. Lee received the Society of Automotive Engineering's Ralph R. Teeter Education Award (1985), Virginia Tech's Alumni Award for Research Excellence (1990), and its College of Engineering Dean's Award for Excellence in Research (1997), the William E. Newell Power Electronics Award in 1989, the highest award presented by the IEEE Power Electronics Society for outstanding achievement in the power electronics discipline, the Power Conversion and Intelligent Motion Award for Leadership in Power Electronics Education (1990), the Arthur E. Fury Award for Leadership and Innovation in Advancing Power Electronic Systems Technology (1998), the IEEE Millennium Medal, and honorary professorships from Shanghai University of Technology, Shanghai Railroad and Technology Institute, Nanjing Aeronautical Institute, Zhejiang University, and Tsinghua University. He is an active member in the professional community of power electronics engineers. He chaired the 1995 International Conference on Power Electronics and Drives Systems, which took place in Singapore, and co-chaired the 1994 International Power Electronics and Motion Control Conference, held in Beijing. During 1993–1994, he served as President of the IEEE Power Electronics Society and, before that, as Program Chair and then Conference Chair of IEEE-sponsored power electronics specialist conferences.



Peng Xu (S'00) was born in Zhejiang, China, in 1973. He received the B.S. and M.S. degrees in electrical engineering from Zhejiang University, Hangzhou, China, in 1994 and 1997, respectively, and is currently pursuing the Ph.D. degree in power electronics at the Center for Power Electronics Systems (CPES), Virginia Polytechnic Institute and State University, Blacksburg.



Bo Yang received the B.Eng. and M.Sc. degrees from Tsinghua University, Beijing, China, in 1994 and 1997, respectively.

He joined the Virginia Power Electronics Center (VPEC), Blacksburg, in 1997 as a Graduate Research Assistant. His research interests include PWM dc/dc converter, resonant dc/dc converter, and power semiconductors.